S bridging active centers coordination with oxygen vacancy of metastable blue WO$_3$ for efficient C–C coupling and highly selective photoconversion CO$_2$ to ethylene

Lijun Xiong [a], Yingjie Hu [c], Yang Wang [a], Wei Dong [a], Xiaoyue Zhang [b], Kan Zhang [d,*], Tianyu Wang [b], Jinyou Shen [b], Yong Yang [a,*]

[a] School of Chemistry and Chemical Engineering, Nanjing University of Science and Technology, Nanjing 210094, PR China
[b] Key Laboratory of Environmental Remediation and Ecological Health, Ministry of Industry and Information Technology, School of Environmental and Biological Engineering, Nanjing University of Science and Technology, Nanjing 210094, China
[c] Nanjing Key Laboratory of Advanced Functional Materials, Nanjing Xiaozhuang University, Nanjing 211171, PR China
[d] School of Materials Science and Engineering, Nanjing University of Science and Technology, Nanjing 210094, PR China

ARTICLE INFO

ABSTRACT

This study proposes that metastable WO$_3$ exhibits efficient photoconversion of CO$_2$ to ethylene (C$_2$H$_4$). It is found that 1) the metastable hexagonal WO$_3$ (h-WO$_3$) offers a suitable bandgap for CO$_2$ reduction, and its surface oxygen vacancy can enhance the light absorption capability and promote the separation of photogenerated electron-hole pairs, simultaneously; 2) S atoms replace oxygen atoms as the bridges to connect the adjacent W atoms to form W-S-W sites are beneficial to adsorb the *CH$_2$ intermediates. Consequently, the optimized h-WO$_3$ nanorods integrating oxygen vacancy and sulfur doping together have achieved the C$_2$H$_4$ generation yield of 1121.39 µmol g^{-1} with the record-high yield-based selectivity of 87.6% and electron-based selectivity of 95.7% in the field of photocatalytic CO$_2$ reduction so far. This work provides a new avenue for the realization of CO$_2$ photoconversion to C$_{2+}$ products on a single metal oxide by virtue of O vacancy and S doping synergistic utilization.

1. Introduction

Multi-carbon products are important chemical raw materials and fuels with high added value. While CO$_2$ can be converted into multi-carbon products through catalytic hydrogenation and carbon-carbon coupling reaction, making CO$_2$ a significant carbon resource for synthesis of multi-carbon products. [1–3] However, the formation of carbonaceous (C$_{2+}$) chemicals is severely limited due to the difficult step of C-C coupling, including multi-electrons/protons transfer and sluggish kinetics. [4–6] Among them, olefiant gas (ethylene, C$_2$H$_4$) accounts for about 75% of the raw materials for petrochemical production, which is mainly generated under harsh production conditions (800–900 °C) with huge challenges. [7,8] The high demand for C$_2$H$_4$ and the high energy consumption during production stimulate the enthusiasm for exploration of a mild, environment-friendly approach to generate C$_2$H$_4$. The photoreduction of CO$_2$ can be realized under mild condition, which is regard as a feasible method to produce carbonaceous chemicals like C$_2$H$_4$. [9,10] Nevertheless, the low yield and poor selectivity of photocatalytic C$_2$H$_4$ production seriously limit its practical application. Nowadays, copper-based catalysts and noble metal catalysts mainly contribute to the generation of C$_{2+}$ products under light irradiation. [11–13] However, the coordination environment of the catalysts and the mechanism of the active site in the stabilized reaction intermediates have not been thoroughly studied. Meanwhile, the activity and selectivity are not satisfactory. Therefore, it is urgent to explore more highly efficient photocatalysts with low cost that can realize high-efficiency photocatalytic C$_2$H$_4$ production.

Tungsten oxide (WO$_3$), with appropriate valence band potential, is widely used in the field of photocatalytic oxidation reactions. [14,15] While pure WO$_3$ photocatalyst is difficult to realize photocatalytic CO$_2$ reduction because of the unsatisfied conduction band position. Besides, the WO$_3$ photocatalyst with the blue color of the metastable state is rare to be studied not to mention in photoreduction of CO$_2$. The blue color is attributed to the W^{6+} reduction to W^{5+} or W^{4+}, the color deepens with

* Corresponding authors.
E-mail addresses: zhangkan@njust.edu.cn (K. Zhang), yychem@njust.edu.cn (Y. Yang).

the increase of reduced state which indicates the existence of O vacancies. [16] Meanwhile, the abundant oxygen vacancies can induce internal lattice strain in WO_3, which adjusts the energy band alignment and optimize the photoinduced charge behavior of the catalysts. [17,18] The metastable state caused by surface oxygen vacancy leads to the formation of high-energy surface that is conducive to enhance the adsorption of visible light and improve the light-induced charge separation efficiency. However, the blue metastable WO_3 has not yet been applied in the field of photocatalytic CO_2 reduction. Besides building oxygen vacancy, the strategy of doping has been proved to introduce the defect energy level and change the photoelectric performance. [19,20] Xie et al. supposed a photocatalyst of CuACs/PCN to tailor the intermediate energy levels and the surrounding doped P promotes the generation of C_2H_4. [21] Meanwhile, Chen et al. also reported the S-modulated $Fe-N_4$ catalyst for the conversion of CO_2 to *COOH with a proton feeding effect. [22] Liang et al. presented W^{6+}-doping introduced $W-N_6$ as multifunctional active sites which catalyzed the selective conversion into hydrocarbons by reducing reaction barriers and moderately stabilizing CO intermediates. [23] To some extent, it proves the role of doping in promoting C-C coupling. Generally, the strategy of introducing defects into photocatalysts for improving the activity and selectivity of C_{2+} products generation has been studied and the surface oxygen vacancies (V_o) can increase the CO_2 adsorption energy, which facilitates the adsorption and activation of CO_2 molecules on the photocatalyst surface. [24,25] Therefore, more electrons are concentrated on the reduction sites, which further improves the possibility of excellent photocatalytic CO_2 reduction activity. However, few studies have reported the combination of doping and vacancy in the WO_3 system for the collaborative conversion of CO_2 to C_{2+} products.

Herein, for the first time, a series of metastable WO_3 photocatalysts with the coexistence of S doping and O vacancy have been prepared through a one-step hydrothermal method. The as-obtained WO_3 presents a fascinating blue color with metastable features, which present a superior C_2H_4 yield and selectivity towards CO_2 photoconversion. In particular, the C_2H_4 yield on O_v-WO_3-THU reaches 1121.39 μmol g^{-1} with 87.6% yield-based selectivity and 95.7% electron-based selectivity. While the apparent quantum efficiency of O_v-WO_3-THU has reached 1.4% at 365 nm. Both density functional theory (DFT) calculations and in-situ DRIFTS measurement indicate that the W atoms act as the reactive sites for CO_2 activation and *CH_2 generation. And S atoms acting as the bridge of W-S-W sites pull W atoms closer for C-C coupling, which significantly reduces the energy barrier for this rate-determining step of C_2H_4 production. Meanwhile, the metastable state caused by surface oxygen vacancy can promote light absorption, which improves the separation of photogenerated electrons and holes and allows more electrons to concentrate on the S atoms and participate in the C-C coupling step. This work provides a new avenue for the realization of CO_2 photoconversion to C_{2+} products on a single metal oxide by O vacancy and S doping synergistic utilization.

2. Experimental section

2.1. Preparation of O_v-WO_3 catalysts

O_v-WO_3-THU was synthesized through a simple one-step hydrothermal method. 2 mmol Na_2WO_4•2 H_2O and 4 mmol CH_4N_2S were mixed in the solution of 80 mL deionized water and 4 mL acetic acid, stirred vigorously for 30 min. Subsequently, the mixture was added to a hydrothermal kettle and heated at 200 ℃ for 20 h. Then the temperature dropped to room temperature and centrifuged with deionized water and ethanol for 3 times and freeze-dried to gain the blue O_v-WO_3 powder. Similarly, O_v-WO_3-AT, O_v-WO_3-TAA and O_v-WO_3-U can be synthesized through the same method using NH_4SCN, CH_3CSNH_2 and CH_4N_2O as precursors.

2.2. Materials characterization

X-ray diffraction (XRD) analysis was conducted on a Bruker-AXS D8 Advance X-ray diffractometer equipped with Cu Kα radiation at 40 kV and 40 mA. Scanning electron microscopy (SEM) images were recorded on JSM-IT500HR with an energy-dispersive X-ray spectroscopy (EDX). Transmission electron microscopy (TEM) and high-resolution TEM images were gained on Tecnai G2 F30 S-Twin microscope with accelerating voltage of 200 kV. X-ray photoelectron spectroscopy (XPS, PHI QUANTERA II) was used with C1s at 284.6 eV as calibration reference. The diffuse reflectance spectra were recorded on Shimadzu UV-2600 spectrometer over the range of 250–1500 nm. Electron paramagnetic resonance (EPR) spectra were measured on Bruker A300–10/12. CO_2 adsorption measurements were conducted on ASAP 2460. Brunauer-Emmett-Teller (BET) specific surface area was gained by ASAP 2020 PLUS HD88 at 77 K through nitrogen adsorption-desorption isotherm. *In-situ* DRIFTS characterization was performed on FT-IR-6300 spectrometer using CO_2 as carrier gas. The photocatalytic CO_2 reduction products were detected by a gas chromatography with FID and TCD detectors (GC-2014 C, Shimadzu Corp., Japan). Isotope testing of $^{13}CO_2$ and $H_2^{18}O$ was measured on a gas chromatography-mass spectrometry (QP2010SE, Shimadzu Corp., Japan). The apparent quantum efficiency was measured and the light intensity of the monochromatic light was obtained by a photometer (Newport, 840 C). CO temperature programmed desorption (CO-TPD, ChemiSorb 2750) measurement was conducted to illustrate the combination binding ability of CO and photocatalysts. Thermogravimetric analysis-differential scanning calorimetry (TGA-DSC, Mettler Toledo TGA/DSC1) tests were measured to evaluate the change of mass and heat quantity with temperature. Raman spectrum was exhibited by the Aramis instrument with the excitation wavelength at 532 nm.

2.3. Photocatalytic CO_2 reduction to ethylene

The reaction was conducted on a quartz reactor of total volume about 456 cm^3, and the reaction area was around 4 cm^2 with 20 mg samples evenly distributed on quartz paper, 10 cm away from the light source supported by a 300 W Xenon lamp. 99.999% high purity CO_2 was pumped into the reactor for 30 min to achieve the adsorption equilibrium. While 0.4 mL of deionized water was injected to provide H protons to participate in the generation of hydrocarbons. Subsequently, the system was irradiated and 1 mL of gas was taken out every 1 h for analysis using a gas chromatography and the reaction lasted for 5 h.

2.4. Electrochemical tests

The photoelectrochemical tests were conducted on CHI760E electrochemical workstation with a standard three-electrode system. The samples were prepared by 10 mg O_v-WO_3, 0.5 mL ethanol, 0.5 mL water and 10 μL Nafion solution. Then the solution was ultrasonically dispersed and coated on ITO conductive glasses as working electrode. While Pt and Ag/AgCl electrodes were worked as auxiliary electrode and reference electrode. 0.1 M Na_2SO_4 solution was used as electrolyte.

2.5. In-situ DRIFTS measurement

The samples and a few drops of water were put on the test bench. Firstly, the system was purged with CO_2 for 30 min in the dark. Then, introducing the light source and collecting the signal every 10 min for an hour.

2.6. Isotope labeling test

20 mg of the photocatalyst was added into the 50 mL quartz tube with 0.2 mL $H_2^{18}O$ injected into the system. The tube was vacuumed and pumped $^{13}CO_2$ as the reaction atmosphere. Then the system was

irradiated under the 300 W Xenon lamp and the gas was brought out and analyzed by a gas chromatography-mass spectrometry.

3. Results and discussion

A series of O_v-WO_3 photocatalysts were prepared through a one-step hydrothermal method and the diagram of reaction was supplemented in Fig. 1a. As a result, the WO_3 photocatalyst appears as dark blue or baby blue with or without S doping in Fig. S1. The structural model diagrams of S-O_v-WO_3 (top view and side view) are shown in Fig. 1b. It can be clearly seen that the introduced S atoms play a important role in connecting the W atoms to shorten the distance between adjacent W atoms. Besides, the charge density difference of S-O_v-WO_3 compared to O_v-WO_3 is exhibited in Fig. 1c, the electrons are transferred from W atoms to S atoms to form electron aggregation on W-S-W bridges, which is conducive to the subsequent photocatalytic reduction of CO_2 and provides active sites for the reaction. Therefore, it is necessary to develop a WO_3 catalytic system that combines O vacancies and S doping to efficiently provide active sites and improve reaction activity.

The related SEM images of O_v-WO_3 were exhibited in Fig. 2. As for O_v-WO_3-AT, it appears as a pine tree which is composed of the main trunk as the center and the branches diverge from the center (Fig. 2a). Meanwhile, the O_v-WO_3-THU and O_v-WO_3-TAA all exhibit the similar morphologies of pine tree (Figs. 2b-2c). Besides, the O_v-WO_3-U shows different morphology like the nanorods (Fig. 2d). Otherwise, the Energy Dispersive Spectrometer (EDS) images of O_v-WO_3 were exhibited in Fig. S2-Fig. S5. All four O_v-WO_3 photocatalysts conclude the elements of W, O, S except for O_v-WO_3-U which only contains W, O elements without any sulfur source. The elements distribute uniformly and the element content of S is the least which evenly disperses on the surface of WO_3.

What's more, the transmission electron microscope (TEM) images of O_v-WO_3-AT show a more obvious rootstock structure and the trunks are about 200 nm while the branches are around 50 nm (Fig. 2e). Through the high-resolution transmission electron microscope (HRTEM) image, the lattice spacing of 0.317 nm can be assigned to the crystal face (200) of hexagonal WO_3. [26] The related HAADF image and elemental mapping images of O_v-WO_3-AT exhibited the uniform distribution of W, O, and S elements (Fig. 2f). Besides, the trunk of O_v-WO_3-THU exhibits a nanowire and the length diameter ratio is over 10:1 (Fig. 2 g). Similarly, the lattice spacing is measured of 0.317 nm with many disorder areas and the partial lattice stripes are very vague that can be attributed to the formation of oxygen vacancy clusters. [27] The additional TEM images of O_v-WO_3 were showed in Fig. S6-Fig. S9. Besides, the relative HAADF image and elements distribution of O_v-WO_3-THU contains W, O, and S elements which are evenly distributed along with the structure (Fig. 2h). The main exposed crystal faces of O_v-WO_3-TAA and O_v-WO_3-U were the same and the lattice spacing of 0.375 nm can be assigned to (110) crystal face of hexagonal WO_3 (Fig. 2i and Fig. 2k). [28] The different main exposed facet may influence the subsequent adsorption and activation of CO_2. Since the charge transfer rate exhibits difference at various facets and affects the reaction activity. The additional HRTEM images of O_v-WO_3 were added in Fig. S10-Fig. S13. The HAADF images and EDS mapping of O_v-WO_3-TAA displayed W, O, and S elements and O_v-WO_3-U exhibited that the W and O elements are uniformly distributed on the catalysts (Fig. 2j, Fig. 2l, Fig. S14-S15).

To further observe the composition of the prepared photocatalysts, the X-ray diffraction (XRD) patterns (Fig. 3a) show that the main content of the photocatalyst is hexagonal WO_3 with diffraction peaks at 13.8° (100), 22.8° (002), 24.2° (110), 28.1° (200) and 36.5° (202) which correspond to the PDF card (JCPDS 85–2459). [29] It is universally
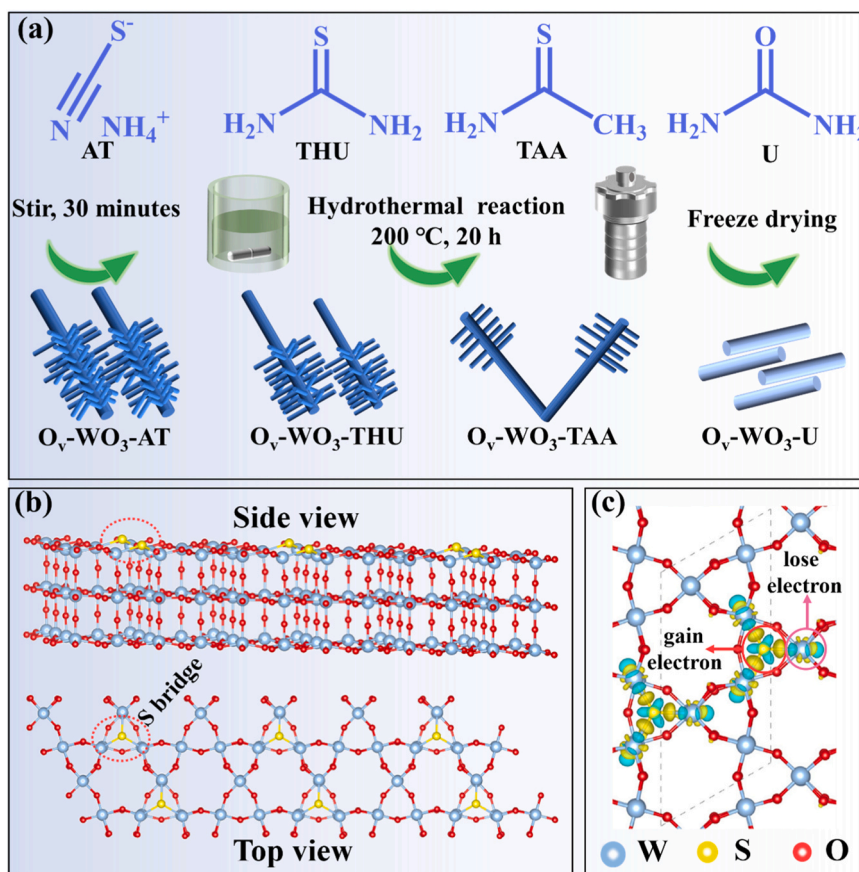
Fig. 1. (a) Synthetic illustration of photocatalysts, (b) The crystalline models of S-O_v-WO_3 from top and side views, (c) charge density difference of S-O_v-WO_3 compared to O_v-WO_3 (The yellow portion represents electron aggregation, the green portion represents electron loss).
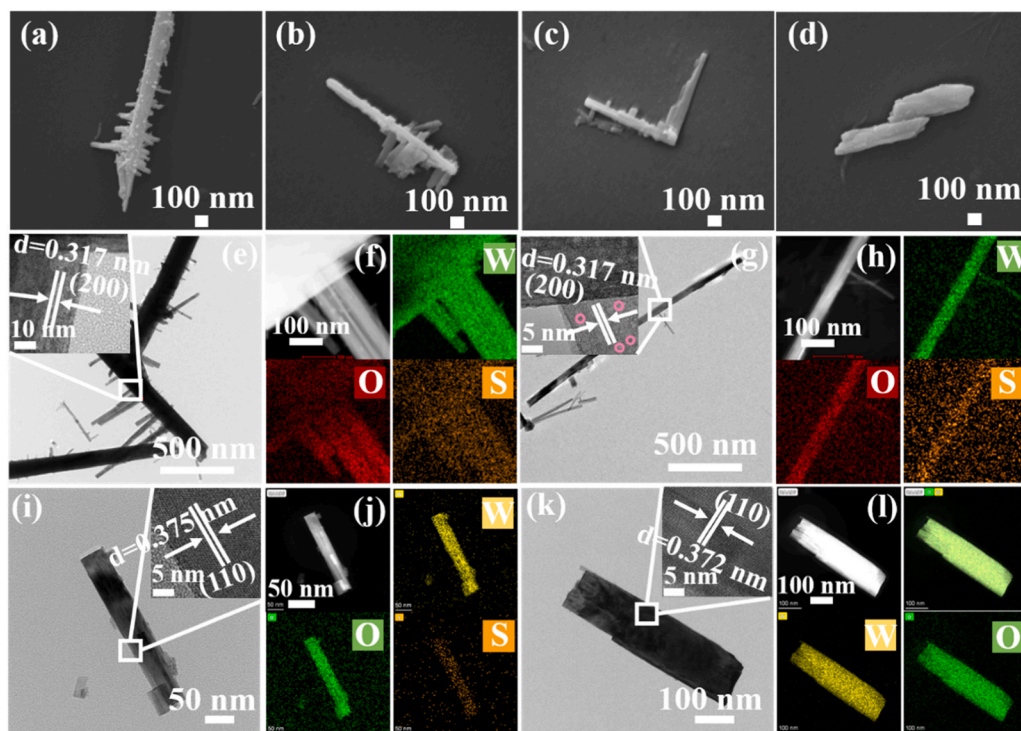
Fig. 2. (a-d) SEM images of O_v-WO$_3$-AT, O_v-WO$_3$-THU, O_v-WO$_3$-TAA and O_v-WO$_3$-U, (e) TEM image of O_v-WO$_3$-AT (HRTEM image of the selected area), (f) HAADF image and EDS elemental mapping images of O_v-WO$_3$-AT, (g) TEM image of O_v-WO$_3$-THU (HRTEM image of the selected area), (h) HAADF image and EDS elemental mapping images of O_v-WO$_3$-THU. (i) TEM image of O_v-WO$_3$-TAA (HRTEM image of the selected area), (j) HAADF image and EDS elemental mapping images of O_v-WO$_3$-TAA, (k) TEM image of O_v-WO$_3$-U (HRTEM image of the selected area), (l) HAADF image and EDS elemental mapping images of O_v-WO$_3$-U.

known that hexagonal phase WO$_3$ is mainly composed of metastable crystalline phases. Compared with O_v-WO$_3$-U, the crystallinity of the S-doped WO$_3$ is significantly improved. As for O_v-WO$_3$-TAA, the (100) peak shifts to higher angles, indicating the contraction of the interlayer owing to a strong van der Waals and the intensity of (002) peak decreases which can be ascribed to the larger atomic radius of the inserted S or S atoms located between the neighboring layers. [30] Besides, the blue WO$_3$ photocatalysts represent the unique color and owned abundant O vacancies detected by Electron paramagnetic resonance (EPR) measurement (Fig. 3b). While the g≈2.003 ± 0.001 can be assigned to oxygen vacancies [31] on WO$_3$ surfaces. Meanwhile, based on the X-ray photoelectron spectroscopy (XPS) test, it can be seen that the amount of S atoms introduced to O_v-WO$_3$-TAA is the highest, and the unpaired electron response is the strongest, indicating that excessive introduction of electronic charges may cause lattice distortion of O_v-WO$_3$-TAA. The XPS results exhibit that both of the O_v-WO$_3$ nanorods all conclude W$4f$ and O$1s$ (Fig. 3c). The W$4f$ high-resolution spectrum of O_v-WO$_3$ shows doublet at 38 eV and 35.8 eV which are assigned to the binding energies of the W$4f_{5/2}$ and W$4f_{7/2}$. It can be attributed to W^{6+} ions while the binding energies of 34.4 eV and 36.6 eV correspond to W$4f_{7/2}$ and W$4f_{5/2}$ of W^{5+} ions (Fig. 3d). [32] The metastable state and multiple valence states of the photocatalysts provide more active sites and promote photocatalytic activity. The O$1s$ spectra of O_v-WO$_3$ are deconvoluted into three peaks, which are assigned to lattice oxygen (530.5 eV), vacancy oxygen (531.3 eV) and hydroxyl groups (OOH) (532 eV) in Fig. 3e. [33] Meanwhile, the S$2p$ shows in Fig. 3f and the S element exists in all the O_v-WO$_3$ photocatalysts except for O_v-WO$_3$-U. The binding energy of S distributed at 168 eV is assigned to the S-O band because of the partial oxidation of the surface S substance. The binding energies divide into two peaks of 164.5 eV and 162.6 eV can be assigned to S$2p_{5/2}$ and S$2p_{3/2}$ of S^{2-}. [34,35] While the binding energies of S of O_v-WO$_3$-THU slightly decreased that may attribute to the S atoms doped in the lattice of WO$_3$ and the electrons accumulated on S atoms. Besides, Raman spectra proposed in Fig. S16 illustrate that the photocatalysts are basically composed of pure WO$_3$. In order to further prove the enhanced adsorption ability to introduce heteroatoms into the photocatalysts. The absorption capacity of the catalysts was exhibited in Fig. 3g, and.

the strong absorption appeared in the ultraviolet and visible light regions while the oxygen vacancies may contribute to the visible light region absorption. [36] Generally, the bandgap is determined by UV-Vis diffuse reflectance after the conversion of the Kubelka-Munk function versus photon energy (insert in Fig. 3g). Firstly, the O_v-WO$_3$-THU exhibits the strongest absorption capability with the darkest color. While the light absorption capacities of O_v-WO$_3$-AT and O_v-WO$_3$-TAA are close while O_v-WO$_3$-U displays the weakest ability of light absorption. The bandgaps of the photocatalysts are obtained by the formula as follows: $\alpha h\upsilon = A (h_\upsilon - E_g)^2$. The calculated bandgap of O_v-WO$_3$-THU, O_v-WO$_3$-AT, O_v-WO$_3$-TAA and O_v-WO$_3$-U is 2.31 eV, 2.54 eV, 2.40 eV and 2.49 eV, respectively. Besides, according to the XPS valence band spectra (Fig. 3h), the energy levels of VB of the photocatalysts are determined to be about 2.75 eV, 2.79 eV, 2.77 eV and 2.57 eV below the Fermi level. Furthermore, through the Mott-Schottky measurements (Fig. S17), the Fermi level of O_v-WO$_3$-THU/AT/TAA/U is estimated to be − 0.81 eV, − 0.94 eV, − 0.96 eV and − 0.84 eV (vs. NHE). Therefore, the valence band positions of O_v-WO$_3$-THU/AT/TAA/U are calculated to be 1.76 eV, 1.85 eV, 1.81 eV and 1.91 eV, respectively. Moreover, the conduction band can be calculated according to the formula: $E_g = E_{VB} - E_{CB}$. The conduction band of O_v-WO$_3$-THU/AT/TAA/U is − 0.55 eV, − 0.69 eV, − 0.59 eV and − 0.58 eV, respectively (Table S1). Consequently, the potentials of conduction band positions are satisfied to the CO$_2$ reduction (CO$_2$/CO: −0.53 V vs NHE, CO$_2$/CH$_4$: −0.24 V vs NHE, CO$_2$/C$_2$H$_4$: 0.06 V vs NHE), [37] which meets the requirement for thermodynamics and the energy level structure diagrams of O_v-WO$_3$ are shown in Fig. 3i. Generally, WO$_3$ photocatalysts are mainly applied in oxidation reactions. In this work, the S doping has changed the band structure and broadened the conduction band to meet the potential of CO$_2$ reduction to some extent. [38]

To evaluate the activity of the photocatalysts, photocatalytic CO$_2$ reduction measurements were performed under the irradiation of a 300 W Xenon lamp and the introduced H$_2$O providing H protons to participate in the reduction reaction. It is pleasantly surprising to find that the O_v-WO$_3$-THU exhibits the highest activity of photocatalytic CO$_2$ reduction (Fig. 4a). Especially, the production of C$_2$H$_4$ over 5 h reaches 1121.39 μmol g^{-1}, and the yield of CH$_4$, CO is 47.86 μmol g^{-1} and
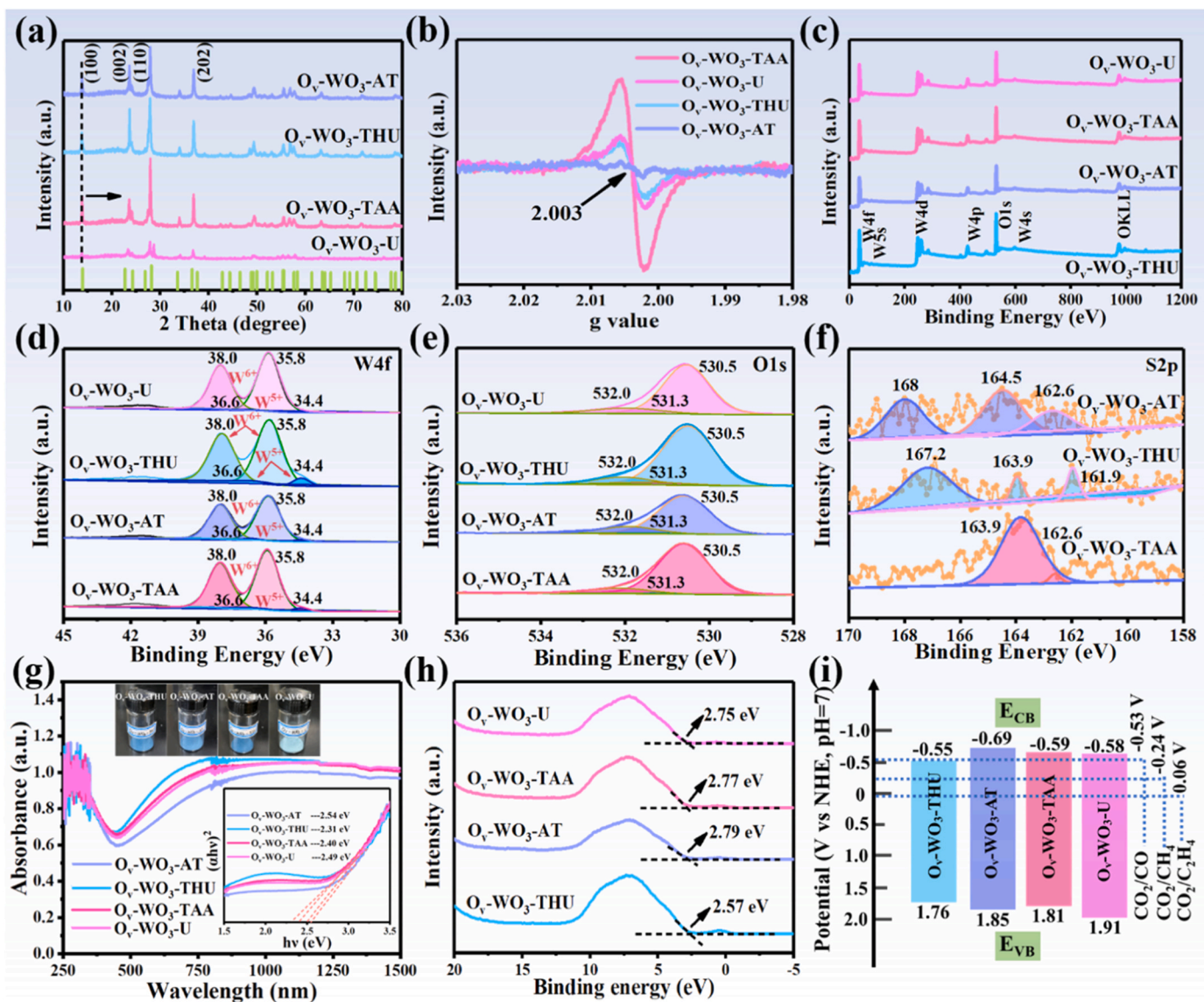
Fig. 3. (a) XRD patterns of the prepared photocatalysts, (b) EPR spectra of O_v-WO_3. (c) XPS survey spectra of O_v-WO_3. (d, e, f) High-resolution XPS spectra of W*4f*, O*1s* and S*2p* of S doped- WO_3. (g) UV-Vis DRS spectrogram (insert: Corresponding plots of transformed Kubelka-Munk function versus photon energy for prepared samples.) (h) XPS-valence band of prepared samples. (i) Energy level structure diagrams of the O_v-WO_3.

111.08 μmol g^{-1}, respectively. O_v-WO_3-THU represents 87.6% yield-based selectivity and 95.7% electron-based selectivity of C_2H_4. [39] Meanwhile, O_v-WO_3 with other precursors exhibits inferior activity in generating the products of C_2H_4, CH_4 and CO. The yield of C_2H_4 of O_v-WO_3-AT, O_v-WO_3-TAA and O_v-WO_3-U is 79.64 μmol g^{-1}, 72.38 μmol g^{-1} and 27.25 μmol g^{-1}. (Fig. S18-Fig. S20). However, the pure WO_3 composed of a monoclinic phase refers to previous work without O vacancy and S doping has extremely low photocatalytic CO_2 reduction activity and generates no C_{2+} products compared to the metastable hexagonal phase WO_3 in this article. (Fig. S21). The production rate based on time is exhibited in Fig. 4b. The excellent C_2H_4 yield of O_v-WO_3-THU can be intuitively observed. Meanwhile, the yield selectivity of C_2H_4 of O_v-WO_3-AT, O_v-WO_3-TAA and O_v-WO_3-U is 75.0%, 57.2% and 39.9%, respectively (Table S2). Besides, to evaluate the stability of the photocatalysts, the cyclic stability of O_v-WO_3-THU has been measured over 20 h for four cycles. The activity of C_2H_4 has an insignificant decrease compared to the original activity (Fig. 4c). Meanwhile, to further prove the stability of the photocatalysts, the XRD patterns before and after photocatalytic CO_2 reduction are exhibited in Fig. S22 and there is no significant difference between the same

material. Furthermore, conditional control experiments were conducted to study the requirements for the reaction (Fig. S23). As a result, light, photocatalyst and CO_2 gas are indispensable for photoreduction of CO_2. To verify the generation of C_2H_4 originated from the introduced CO_2, an isotope labeling experiment using $^{13}CO_2$ as reaction gas instead of $^{12}CO_2$ was measured. (Fig. 4d). Consequently, all the products including CH_4, CO and C_2H_4 are generated from the photocatalytic CO_2 reduction. Excluding the possibility that the adsorbed carbonous pollutants on the photocatalyst release these products. Besides, the products in the photocatalytic reaction of $^{13}CO_2$ were observed in the GC detector (Fig. 4e). It is obvious that the products contained ^{13}CO, $^{13}CH_4$ and $^{13}C_2H_4$ from $^{13}CO_2$ according to the different retention times. While ^{13}CO peak (1.25 min) appears earlier than $^{13}CH_4$ (1.30 min), $^{13}CO_2$ (1.60 min) and $^{13}C_2H_4$ (2.10 min). The above results indicate that all the products in the reaction process are generated from the reduction of CO_2. In addition, the product of oxidation $H_2^{18}O$ appears in the GC trace. Moreover, when $H_2^{18}O$ was introduced instead of $H_2^{16}O$, $^{18}O_2$ ($m/z = 36$), $^{18}O^{16}O$ ($m/z = 34$) and $^{16}O_2$ ($m/z = 32$) were detected, indicating that the produced $^{18}O_2$ is derived from the oxidation of $H_2^{18}O$ (Fig. 4f). [40,41] In the photocatalytic CO_2 reduction system, oxygen was generated from
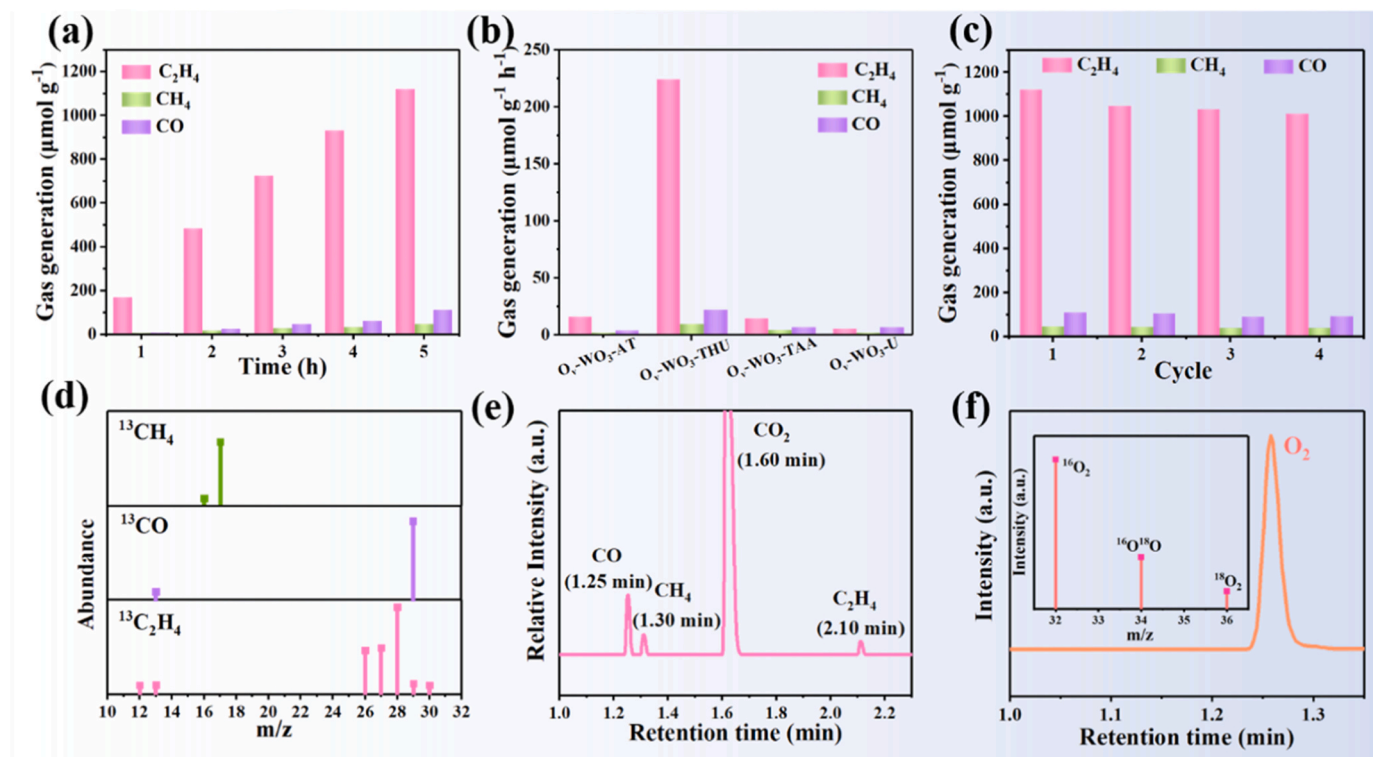
Fig. 4. (a) The yield of CO, CH$_4$ and C$_2$H$_4$ of O$_v$-WO$_3$-THU, (b) CO, CH$_4$ and C$_2$H$_4$ generation rate of O$_v$-WO$_3$, (c) Stability test of O$_v$-WO$_3$-THU with 5 h as a cycle for 4 cycles. (d) Isotope experiment with ^{13}CO$_2$ as gas source, (e) GC traces of ^{13}CO, ^{13}CH$_4$ ^{13}CO$_2$ and ^{13}C$_2$H$_4$, (f) GC traces of O$_2$ (insert: MS spectra of the products in the photocatalytic reaction of H$_2^{18}$O).
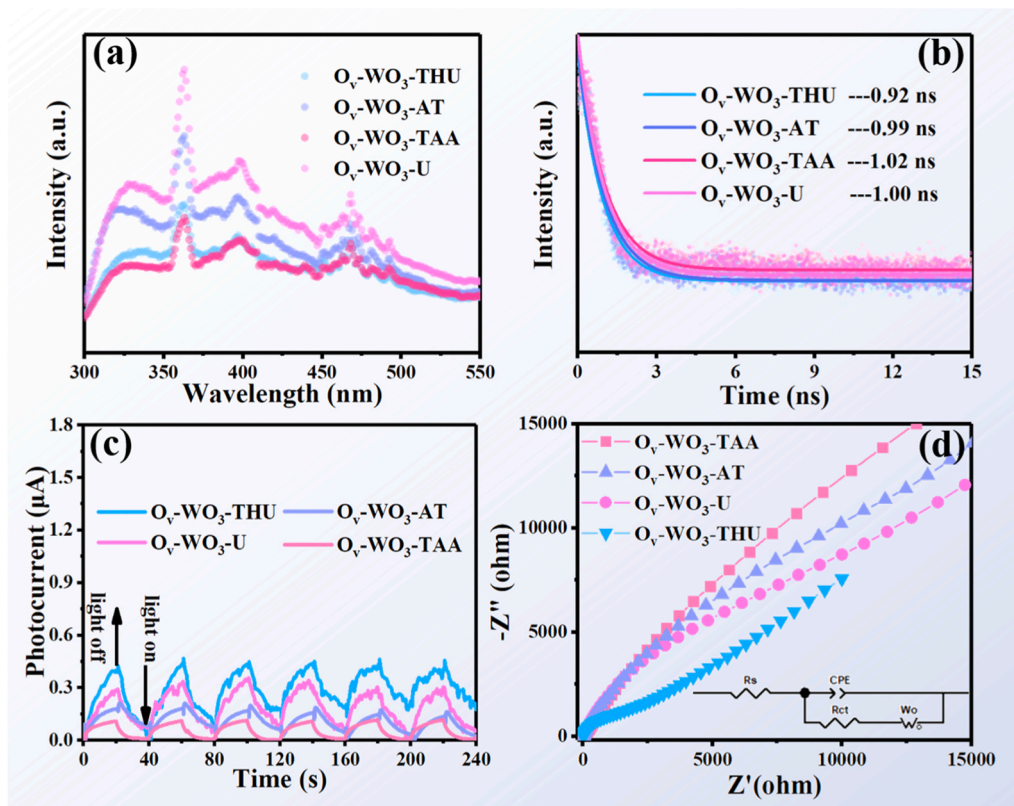
Fig. 5. (a) Photoluminescence spectroscopy of O$_v$-WO$_3$, (b) Time-resolved emission decay spectra of O$_v$-WO$_3$, (c) Transient photocurrent responses of O$_v$-WO$_3$, (d) Electrochemical impedance spectra (EIS) of O$_v$-WO$_3$ (insert: equivalent circuit).

the oxidation reaction while the hydrogen evolution was regarded as the competitive reaction. The yields of O_2 and H_2 are detected and compared with the yield of CO in Fig. S24. In particular, the apparent quantum efficiency (AQE) of O_v-WO_3-THU at 365 nm, 420 nm and 520 nm is 1.40%, 0.90% and 0.39% (Fig. S25). The relative measurement and information of the incident light were shown in Table S3.

As observed in the steady-state photoluminescence (PL) spectroscopy of the samples (Fig. 5a). O_v-WO_3-U exhibits a stronger emission peak than O_v-WO_3-AT while O_v-WO_3-THU and O_v-WO_3-TAA own similar lower emission intensities. Generally, the stronger PL intensity indicated a faster combination of photogenerated charges. [37] Therefore, the recombination rate is obviously suppressed by introducing the S element, thus enhancing the separation efficiency of charges. [38] Besides, to some extent, the high oxygen vacancy content corresponds to the decreased intensity of PL emission. [39] Since O_v-WO_3-TAA owns

the strongest intensity of O vacancy which corresponds to the lowest PL intensity. Meanwhile, the charge migration dynamics on O_v-WO_3 are studied by time-resolved emission decay spectra (Fig. 5b). The average lifetime of O_v-WO_3 is gained through the single exponential fitting. O_v-WO_3-TAA owns the longest lifetime of 1.02 ns while the lifetime of O_v-WO_3-THU shortens to 0.92 ns. It shows that S doping coordination with oxygen vacancy has a significant effect on electron separation. However, such shorter τ_{av} testifies the existence of nonradiative migration pathway for the efficient separation of charges in O_v-WO_3--THU catalyst, in which the charges are transferred quickly. [41] Based on the formula: $k = 1/\tau_{av}$, the charge transfer rate of the O_v-WO_3-THU, O_v-WO_3-AT, O_v-WO_3-TAA and O_v-WO_3-U were 1.087 ns^{-1}, 1.010 ns^{-1}, 0.980 ns^{-1} and 1.000 ns^{-1}, respectively. [42] It indicates the effective suppression of the recombination of photogenerated charges. Meanwhile, the photo-electrochemical tests of photocurrent and
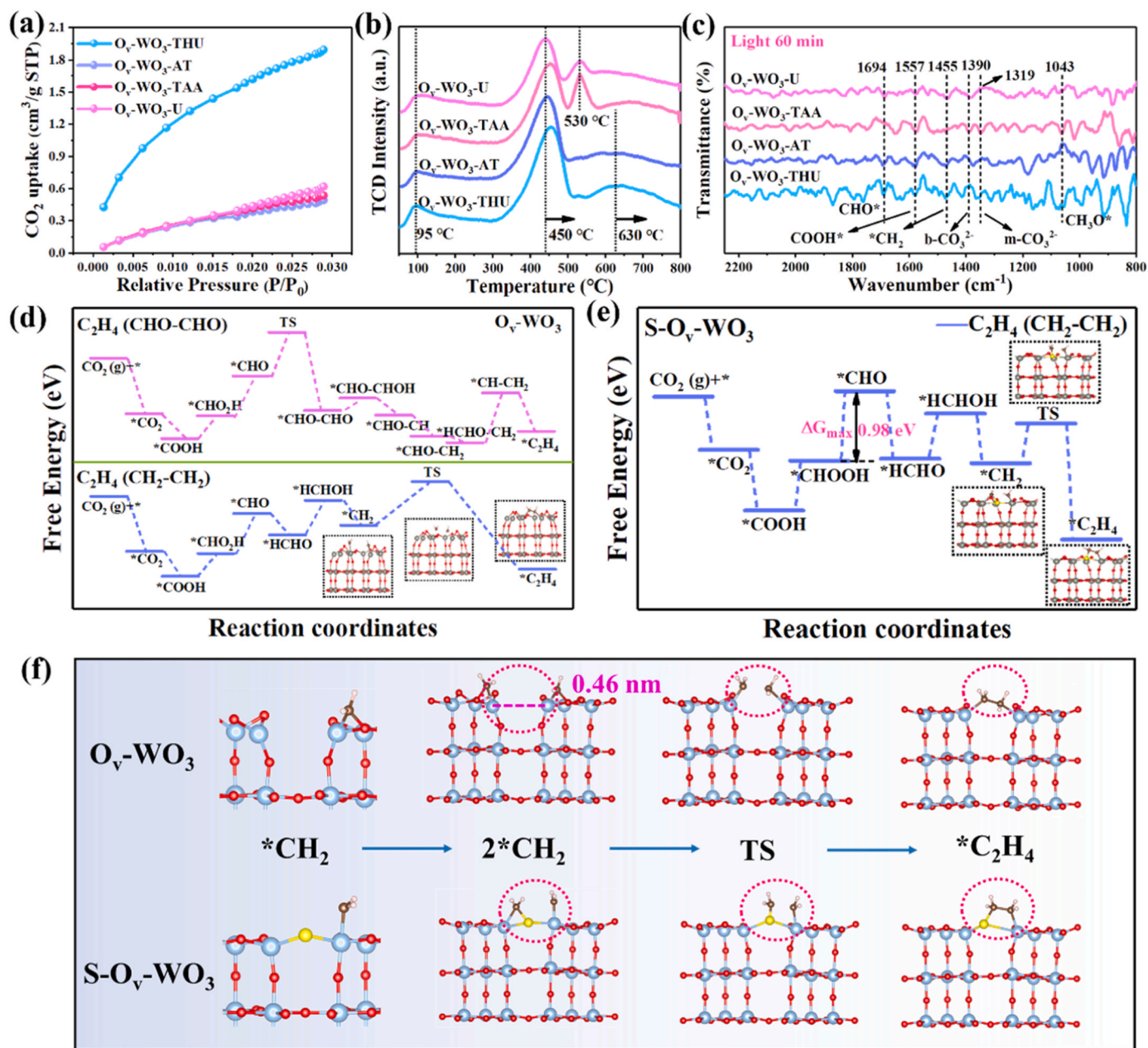

Fig. 6. (a) The CO_2 adsorption isotherms of the O_v-WO_3 samples, (b) CO-TPD of the O_v-WO_3 samples, (c) *In-situ* DRIFTS measurement of the O_v-WO_3 samples, (d) Gibbs free energy diagrams of two kinds of possible C-C coupling pathways over O_v-WO_3, (e) Gibbs free energy diagrams for CO_2 reduction to C_2H_4 over S-O_v-WO_3, (f) The C-C coupling process of O_v-WO_3 and S-O_v-WO_3.

electrochemical impedance spectroscopy (EIS) were carried out to evaluate the capacity of charge transfer (Figs. 5c-5d). The lower charge transfer resistance and a faster charge carrier migration rate in O_v-WO_3-THU, which hinders the photoexcited electron-hole pairs recombination. [43] The equivalent circuit (insert in Fig. 5d) of the device is also applied for the further analysis of the impedance spectra. Rs, CPE, Rct and Wo correspond to the electrolyte solution resistance, constant phase element for the elecrtode and electrolyte interface, interfacial charge transfer resistance and diffusion impedance, respectively. [44] It is obvious that O_v-WO_3-THU has the highest photocurrent intensity and the minimum impedance radius, which all illustrate that more charges are generated and the transfer rate is the fastest corresponding to its highest photocatalytic activity [45,46].

The adsorption ability of CO_2 was evaluated by the CO_2 adsorption isotherms of the samples (Fig. 6a). While the O_v-WO_3-THU exhibits obviously strongest CO_2 adsorption capacity than the other O_v-WO_3. O_v-WO_3-THU shows a promising CO_2 adsorption ability of 1.89 cm^3/g when the P/P_0 is 0.03, which is almost 3–4 times higher than O_v-WO_3-U (0.62 cm^3/g), O_v-WO_3-TAA (0.54 cm^3/g) and O_v-WO_3-AT (0.49 cm^3/g). The excellent CO_2 adsorption capacity is conducive to more CO_2 molecules participating in the reaction. The adsorption amount of CO_2 helps to make CO_2 molecules more effectively contact with the active sites of the photocatalyst, thus increasing the photocatalytic efficiency. [47] Meanwhile, the specific surface area of O_v-WO_3 is measured through N_2 adsorption-desorption isotherms (Fig. S26) which displays the type-IV isotherm with an H3 hysteresis loop and it demonstrates the presence of mesoporous structure in O_v-WO_3. [48] The surface areas of O_v-WO_3--THU/U/TAA/AT are 20.48 m^2/g, 19.15 m^2/g, 15.23 m^2/g and 19.45 m^2/g, respectively. The higher specific surface area may provide more CO_2 adsorption sites to further promote the process of CO_2 activation. Thus further improving the photocatalytic CO_2 reduction. As for O_v-WO_3-TAA, the surface area is the lowest with the highest S doping amount. While the crystallinity of O_v-WO_3-TAA increases, the specific area decreases, and the dispersion of the active components decreases. While the pore diameter of the prepared photocatalysts is mainly distributed between 30 and 50 nm. The pore size distribution curve indicates O_v-WO_3-THU owns more small aperture distribution which corresponds to a higher specific surface area. The pore diameter distribution of O_v-WO_3-THU is near 30 nm and 45 nm while that of other O_v-WO_3 photocatalysts is mainly distributed at about 45 nm (Fig. S27). Besides, the CO temperature programmed desorption (CO-TPD) measurement has been conducted to compare the CO adsorption ability on photocatalysts from room temperature to 800℃ (Fig. 6b). The desorption temperature of CO from photocatalysts can reflect the binding force between CO and the catalyst. The higher desorption temperature corresponds to the more stable CO binding capacity. Therefore, the CO intermediate is more conducive to participate in the next hydrogenation reaction, so as to obtain more C-C coupling product. The adsorption temperature of CO is about 95 ℃, while the desorption temperatures locate at 450 ℃ and 630 ℃ of O_v-WO_3-THU, with the decrease in desorption temperatures of other photocatalysts. Meanwhile, the intensities of the CO desorption peaks of O_v-WO_3-THU are stronger than the other photocatalysts. Both the intensity and the temperature illustrated that the CO tended to adsorb on O_v-WO_3-THU compared to other O_v-WO_3 photocatalysts. The multiple CO intermediates adsorbed on O_v-WO_3-THU may promote the formation of C-C coupling products of C_2H_4. While the TGA test has shown that the materials can remain basically stable at high temperatures (Fig. S28). The slight weight loss at temperatures between 300 ℃ to 500 ℃ may be assigned to some final water decomposition. Generally, the weight of the four photocatalysts did not change significantly over 500 ℃, which indicated that those organics had been removed thoroughly. [49] Otherwise, the possible reaction pathway was proposed with the help of in-situ DRIFTS measurement (Fig. 6c). Since the various intermediates were detected with the increase of irradiation time. When the system is in dark, there is basically no peaks of the intermediates can be observed. The peaks at

1319 cm^{-1} and 1390 cm^{-1} indicate the monodentate carbonate (m-CO_3^{2-}) and bidentate carbonate (b-CO_3^{2-}). [41] The peak locates at 1455 cm^{-1} representing the existence of *CH_2. [12] The peak appearing at 1557 cm^{-1} is assigned to the conversion of COOH* during the CO_2 adsorption process which is considered the key intermediate during the conversion of CO_2 to CO. [50] Meanwhile, the peak locates at 1043 cm^{-1} representing the CH_3O* group, a key intermediate that is important to the formation of C-C bond in the photoreduction of CO_2 to C_2H_4. [51] The peak at 1694 cm^{-1} is assigned to CHO* group since the adsorbed CO_2 was activated. [12] This notably increased peak intensity of *CHO intermediates may participate in further reactions. In view of the existence of *CH_2, *CH_3O and *CHO intermediates, a possible reaction pathway was proposed as *CHO → HCHO* → *CH_3O → *CH_2 → *CH_2-*CH_2 →*C_2H_4. Furthermore, more information of in-situ DRIFTS measurements of the O_v-WO_3 photocatalysts under dark and light are supplemented in Fig. S29, which is evident that the peaks of various intermediates are more pronounced after light irradiation. This not only illustrates the importance of light in the reaction but also verifies the step-by-step reduction reaction after CO_2 adsorption on the surface of the catalyst. Meanwhile, DFT calculations were performed to explore the mechanism toward the generation path of C_2H_4 through CH_2-CH_2 routes of S-O_v-WO_3. While the pathway of *CHO-CHO coupling for S-O_v-WO_3 has been proved infeasible in calculations. Meanwhile, the two pathways of CH_2-CH_2 and CHO-CHO were possible to occur on O_v-WO_3. Firstly, CO_2 molecules are adsorbed on the catalyst surface and H_2O molecules introduced into the system provide hydrogen protons. The free-energy profile for the photocatalytic CO_2 to CO was shown in Fig. S30. For O_v-WO_3, there are two possible paths by CH_2-CH_2 coupling and CHO-CHO coupling, respectively, for the production of C_2H_4 (Fig. 6d). As can be seen, the pathway of CHO-CHO coupling has more steps, and the most important speed determining step of the reaction is the adsorption of CHO intermediates as a transition state on the catalyst surface (1.17 eV). For the CH_2-CH_2 coupling pathway, the determining step is the adsorption of CH_2 as an intermediate transition state on the catalyst surface (1.16 eV). In general, the CH_2-CH_2 path is more conducive to the formation of C_2H_4. Obviously, S-O_v-WO_3 overcomes the lower free-energy barriers than O_v-WO_3. It means that *CO molecules can easily release from the catalyst surface. Besides, the reaction intermediate (*COOH) further couples a proton/electron pair to form *CHOOH. [8] Then the *CHOOH couples a protons/electron pair to generate *CHO and H_2O molecules. This step is regarded as the potential determining step (0.98 eV). Then the intermediates of *CHO gradually added H protons to form *CH_2 and H_2O molecules. Subsequently, the *CH_2 aggregated on the W-S-W, where the S atom occupied the original O vacancy, forming an unstable transition state. Later, the accumulated *CH_2 coupled to generate *CH_2-*CH_2, which desorbed from the catalyst surface to form C_2H_4 (Fig. 6e). Therefore, the in-situ DRIFTS measurement combined with the DFT calculation results, in a possible intermediate transition state reaction pathway of CHO*→ HCHO*→ CH_2OH*→ CH_2 *→ C_2H_4 *→ C_2H_4 is determined. Besides, the CH_4 generation process of O_v-WO_3 and S-O_v-WO_3 is shown in Fig. S31. Overall, the energy barrier of S-O_v-WO_3 from CO_2 to CH_4 is lower than O_v-WO_3, which shows that the formation of CH_4 is easier on S-O_v-WO_3. It can be observed that the electrons accumulate on the S atoms. The S atom occupies the O vacancy as the W-S-W bridge acting as the active site for CH_2-CH_2 coupling. The calculations of the intermediate pathway of CO/CH_4/C_2H_4 generation are supplemented in Fig. S32-S34. Especially in the production of C_2H_4, it is evident that S atoms play an important role in C-C coupling (Fig. 6f). For O_v-WO_3, which exists two possible reaction pathways corresponding to CHO-CHO and CH_2-CH_2 coupling modes. the distance between the adjacent W atoms is 0.46 nm, which is not conducive to C-C coupling. In S-O_v-WO_3, S atoms serve as bridge connections, shortening the distance between W atoms and further promoting the coupling of *CH_2 to generate more C_2H_4.

4. Conclusion

This work provided a mild process to prepare metastable S-doped O_v-WO_3 photocatalysts through a one-step hydrothermal method. Especially, the O_v-WO_3-THU exhibits excellent generation yield of C_2H_4 up to 1121.39 μmol g^{-1} and the yield-based selectivity of C_2H_4 as the major product is up to 87.6% with 95.7% electron-based selectivity. The mechanism of the high activity and selectivity is discussed in the relationship between O vacancy and S doping. Afterwards, the in-situ DRIFTS measurement and DFT calculations are performed to verify the specific reaction pathway and the Gibbs free energy of each reduction step has been determined and evaluated. In this reaction system, the O vacancies provide occupied sites for S atoms which served as the bridges of the adjacent W atoms thus promoting the coupling of $*CH_2$ to form C_2H_4. Therefore, the O vacancy cooperated with S doping is beneficial to CO_2 adsorption and activation. In general, the metastable WO_3 system containing both O vacancy and S doping is instructive in understanding the synergism in the production of C_{2+} products.

CRediT authorship contribution statement

The conceptualization and methodology of the experiment were offered by Lijun Xiong, Yong Yang. They conceived the idea, designed the experiments, and wrote the manuscript. Yingjie Hu performed the theoretical calculations. Yang Wang and Xiaoyue Zhang performed the imaging experiments and data analysis. Tianyu Wang performed the synthesis of O_v-WO_3 photocatalysts. Wei Dong, Kan Zhang and Jinyou Shen, helped with the data analysis and discussion.

Declaration of Competing Interest

The authors declare that they have no known competing financial interests or personal relationships that could have appeared to influence the work reported in this paper.

Data Availability

Data will be made available on request.

Appendix A. Supporting information

Supplementary data associated with this article can be found in the online version at doi:10.1016/j.apcatb.2023.123263.

References

[1] C.B. Hiragond, N.S. Powar, J. Lee, S.I. In, Single-atom catalysts (SACs) for photocatalytic CO_2 reduction with H_2O: activity, product selectivity, stability, and surface chemistry, Small 18 (2022) 2201428, https://doi.org/10.1002/smll.202201428.

[2] H.-N. Shi, H.-Z. Wang, Y.-C. Zhou, J.-H. Li, P.-L. Zhai, X.-Y. Li, G.G. Gurzadyan, J.-G. Hou, H. Yang, X.-W. Guo, Atomically dispersed indium-copper dual-metal active sites promoting C−C coupling for CO_2 photoreduction to ethanol, Angew. Chem. Int. Ed. 61 (2022), e202208904, https://doi.org/10.1002/anie.202208904.

[3] R. Xu, D.-H. Si, S.-S. Zhao, Q.-J. Wu, X.-S. Wang, T.-F. Liu, H. Zhao, R. Cao, Y.-B. Huang, Tandem photocatalysis of CO_2 to C_2H_4 via a synergistic rhenium-(I) bipyridine/copper-porphyrinic triazine framework, J. Am. Chem. Soc. 145 (2023) 8261–8270, https://doi.org/10.1021/jacs.3c02370.

[4] W.-W. Shao, X.-D. Li, J.-C. Zhu, X.-L. Zu, L. Liang, J. Hu, Y. Pan, J.-F. Zhu, W.-S. Yan, Y.-F. Sun, $Metal^{n+}$-$Metal^{\delta+}$ pair sites steer C–C coupling for selective CO_2 photoreduction to C_2 hydrocarbons, Nano Res. 15 (2022) 1882–1891, https://doi.org/10.1007/s12274-021-3789-x.

[5] T. Wang, L. Chen, C. Chen, M.-T. Huang, Y.-J. Huang, S-J. Liu, B.-X. Li, Engineering catalytic interfaces in $Cu^{\delta+}$/CeO_2-TiO_2 photocatalysts for synergistically boosting CO_2 reduction to ethylene, ACS Nano 16 (2022) 2306–2318, https://doi.org/10.1021/acsnano.1c08505.

[6] F.-Y. Yu, X. Jing, Y. Wang, M.-Y. Sun, C.-Y. Duan, Hierarchically porous metal–organic framework/MoS_2 interface for selective photocatalytic conversion of CO_2 with H_2O into CH_3COOH, Angew. Chem. Int. Ed. 60 (2021) 24849–24853, https://doi.org/10.1002/anie.202112604.

[7] L. Wang, B.-H. Zhao, C.-H. Wang, M.-Y. Sun, Y.-F. Yu, B. Zhang, Thermally assisted photocatalytic conversion of CO_2–H_2O to C_2H_4 over carbon doped In_2S_3 nanosheets, J. Mater. Chem. A. 8 (2020) 10175–10179, https://doi.org/10.1039/d0ta01256d.

[8] W. Gao, S. Li, H.-C. He, X.-N. Li, Z.-X. Cheng, Y. Yang, J.-L. Wang, Q. Shen, X.-Y. Wang, Y.-J. Xiong, Y. Zhou, Z.-G. Zou, Vacancy-defect modulated pathway of photoreduction of CO_2 on single atomically thin $AgInP_2S_6$ sheets into olefiant gas, Nat. Commun. 12 (2021) 4747, https://doi.org/10.1038/s41467-021-25068-7.

[9] L.-A. Zhang, T.-L. Liu, T.-F. Liu, S. Hussain, Q.-Y. Li, J.-J. Yang, Improving photocatalytic performance of defective titania for carbon dioxide photoreduction by Cu cocatalyst with SCN- ion modification, Chem. Eng. J. 463 (2023), 142358, https://doi.org/10.1016/j.cej.2023.142358.

[10] M.-P. Kou, W. Liu, Y.-Y. Wang, J.-D. Huang, Y.-L. Chen, Y. Zhou, M.-Z. Ma, K. Lei, H.-Q. Xie, P.K. Wong, L.-Q. Ye, Photocatalytic CO_2 conversion over single-atom MoN_2 sites of covalent organic framework, Appl. Catal. B Environ. 291 (2021), 120146, https://doi.org/10.1016/j.apcatb.2021.120146.

[11] W. Wang, C.-Y. Deng, S.-J. Xie, Y.-F. Li, W.-Y. Zhang, H. Sheng, C.-C. Chen, J.-C. Zhao, Photocatalytic C–C coupling from carbon dioxide reduction on copper oxide with mixed-valence copper(I)/copper(II), J. Am. Chem. Soc. 143 (2021) 2984–2993, https://doi.org/10.1021/jacs.1c00206.

[12] Y.-Y. Yu, X.-A. Dong, P. Chen, Q. Geng, H. Wang, J.-Y. Li, Y. Zhou, F. Dong, Synergistic effect of Cu single atoms and Au–Cu alloy nanoparticles on TiO_2 for efficient CO_2 photoreduction, ACS Nano 15 (2021) 14453–14464, https://doi.org/10.1021/acsnano.1c03961.

[13] Q. Chen, X.-J. Chen, M.-L. Fang, J.-Y. Chen, Y.-J. Li, Z.-X. Xie, Q. Kuang, L.-S. Zheng, Photo-induced Au–Pd alloying at TiO_2 {101} facets enables robust $CO2$ photocatalytic reduction into hydrocarbon fuels, J. Mater. Chem. A 7 (2019) 1334–1340, https://doi.org/10.1039/c8ta09412h.

[14] F.-F. Wang, Z.-M. Yang, Z.-X. Yang, C.-Y. Lu, W. Wang, L. Chen, Y. Shi, C.-D. Chen, Graphene triggered hole activation strategy for 2D/2D-Layered (001)/(100) WO_3 facet junction towards enhanced photocatalytic water oxidation kinetics, Chem. Eng. J. 450 (2022), 138166, https://doi.org/10.1016/j.cej.2022.138166.

[15] Z.-R. Wang, C. Zhu, Z.-T. Ni, H. Hojo, H. Einaga, Enhanced photocatalytic benzene oxidation to phenol over monoclinic WO_3 nanorods under visible light, ACS Catal. 12 (2022) 14976–14989, https://doi.org/10.1021/acscatal.2c03832.

[16] N.M. Makwana, R. Quesada-Cabrera, I.P. Parkin, P.F. McMillan, A. Mills, J.A. Darr, A simple and low-cost method for the preparation of self-supported $TiO2$–$WO3$ ceramic heterojunction wafers, J. Mater. Chem. A. 2 (2014) 17602–17608, https://doi.org/10.1039/c4ta03257h.

[17] K.-R. Wang, L. Luo, C. Wang, J.-W. Tang, Photocatalytic methane activation by dual reaction sites co-modified WO_3, Chin. J. Catal. 46 (2023) 103–112, https://doi.org/10.1016/s1872-2067(22)64169-x.

[18] X.-D. Yang, F. Li, W. Liu, L. Chen, J.-J. Qi, W.-L. Sun, F. Pan, T. Duan, F.-B. Sun, Oxygen vacancy-induced spin polarization of tungsten oxide nanowires for efficient photocatalytic reduction and immobilization of uranium (VI) under simulated solar light, Appl. Catal. B Environ. 324 (2023), 122202, https://doi.org/10.1016/j.apcatb.2022.122202.

[19] Y.-X. Yang, Y.-X. Pan, X. Tu, C.-J. Liu, Nitrogen doping of indium oxide for enhanced photocatalytic reduction of CO_2 to methanol, Nano Energy 101 (2022), 107613, https://doi.org/10.1016/j.nanoen.2022.107613.

[20] Y.-D. Guo, S.-H. Li, F. Yang, C.-X. Li, Y.-P. Guo, K. Xuan, G.-H. Wang, Y.-H. Liu, J. Li, Efficient charge separation in sulfur doped $AgFeO_2$ photocatalyst for enhanced photocatalytic U(VI) reduction: the role of doping and mechanism insights, J. Hazard. Mater. 440 (2022), 129734, https://doi.org/10.1016/j.jhazmat.2022.129734.

[21] W.-K. Xie, K.-J. Li, X.-H. Liu, X. Zhang, H.-W. Huang, P-mediated Cu–N_4 sites in carbon nitride realizing CO_2 photoreduction to C_2H_4 with selectivity modulation, Adv. Mater. 35 (2023) 2208132, https://doi.org/10.1002/adma.202208132.

[22] S.-Y. Chen, X.-Q. Li, C.-W. Kao, T. Luo, K.-J. Chen, J.-W. Fu, C. Ma, H.-M. Li, M. Li, T.-S. Chan, Unveiling the proton-feeding effect in sulfur-doped Fe−N−C single-atom catalyst for enhanced CO_2 electroreduction, Angew. Chem. Int. Ed. 61 (2022), e202206233, https://doi.org/10.1002/anie.202206233.

[23] Y.-J. Liang, X. Wu, X.-Y. Liu, C.-H. Li, S.-W. Liu, Recovering solar fuels from photocatalytic CO_2 reduction over W^{6+}-incorporated crystalline g-C_3N_4 nanorods by synergetic modulation of active centers, Appl. Catal. B Environ. 304 (2022), 120978, https://doi.org/10.1016/j.apcatb.2021.120978.

[24] Y. Hwang, S. Sorcar, J. Lee, J. Jung, C. Cho, S.I. In, Reduced TiO_2 quantum dots/graphene for solar light driven CO_2 reduction into precisely controlled C_1 vs C_2 hydrocarbon products without noble Co-catalyst, J. Power Sources 556 (2023), 232430, https://doi.org/10.1016/j.jpowsour.2022.232430.

[25] T. Phongamwong, M. Chareonpanich, J. Limtrakul, Role of chlorophyll in spirulina on photocatalytic activity of CO_2 reduction under visible light over modified N-doped TiO_2 photocatalysts, Appl. Catal. B Environ. 168 (2015) 114–124, https://doi.org/10.1016/j.apcatb.2014.12.022.

[26] X.-W. Liu, J.-J. Xu, Z.-Y. Ni, R.-C. Wang, J.-H. You, R. Guo, Adsorption and visible-light-driven photocatalytic properties of Ag_3PO_4/WO_3 composites: A discussion of

the mechanism, Chem. Eng. J. 356 (2019) 22–33, https://doi.org/10.1016/j.cej.2018.09.001.

[27] Y.-X. Zhu, X. Zhong, X.-T. Jia, Q.-F. Sun, J.-F. Yao, Geometry-tunable sulfur-doped carbon nitride nanotubes with high crystallinity for visible light nitrogen fixation, Chem. Eng. J. 431 (2022), 133412, https://doi.org/10.1016/j.cej.2021.133412.

[28] T. Sobahi, Visible-light-driven mineralization of atrazine over one-pot-synthesized CuAl$_2$O$_4$-coupled WO$_3$ heterojunction photocatalysts, Appl. Nanosci. 12 (2022) 4059–4068, https://doi.org/10.1007/s13204-022-02639-8.

[29] J. Ding, L. Zhang, Q.-Q. Liu, W.-L. Dai, G.-F. Guan, Synergistic effects of electronic structure of WO$_3$ nanorods with the dominant {001} exposed facets combined with silver size-dependent on the visible-light photocatalytic activity, Appl. Catal. B Environ. 203 (2017) 335–342, https://doi.org/10.1016/j.apcatb.2016.10.028.

[30] Y.-T. Wang, C.-S. Peng, T. Jiang, J. Zhang, Z. Jiang, X.-G. Li, Construction of defect-engineered three-dimensionally ordered macroporous WO3 for efficient photocatalytic water oxidation reaction, J. Mater. Chem. A 9 (2021) 3036–3043, https://doi.org/10.1039/d0ta10803k.

[31] W.-J. Zhang, Y. Hu, L.-B. Ma, G.-Y. Zhu, Y.-R. Wang, X.-L. Xue, R.-P. Chen, S.-Y. Z. Yang, Jin, Progress and perspective of electrocatalytic CO$_2$ reduction for renewable carbonaceous fuels and chemicals, Adv. Sci. 5 (2018) 1700275, https://doi.org/10.1002/advs.201700275.

[32] D. Guo, Y.-Q. Wang, C. Chen, J.-Q. He, M.-L. Zhu, J. Chen, C.-L. Zhang, A multi-structural carbon nitride Co-modified by Co, S to dramatically enhance mineralization of bisphenol fin the photocatalysis-PMS oxidation coupling system, Chem. Eng. J. 422 (2021) 130035, https://doi.org/10.1016/j.cej.2021.130035.

[33] G. Li, X.-X. Deng, P. Chen, X.-D. Wang, J. Ma, F. Liu, S.-F. Yin, Sulphur vacancies-VS$_2$@C$_3$N$_4$ drived by in situ supramolecular self-assembly for synergistic photocatalytic degradation of real wastewater and H$_2$ production: vacancies taming interfacial compact heterojunction and carriers transfer, Chem. Eng. J. 433 (2022), 134505, https://doi.org/10.1016/j.cej.2022.134505.

[34] Y.-N. Bo, H.-Y. Wang, Y.-X. Lin, T. Yang, R. Ye, Y. Li, C.-Y. Hu, P.-Y. Du, Y.-G. Hu, Z. Liu, R. Long, C. Gao, B.-J. Ye, L. Song, X.-J. Wu, Y.-J. Xiong, Altering hydrogenation pathways in photocatalytic nitrogen fixation by tuning local electronic structure of oxygen vacancy with dopant, Angew. Chem. Int. Ed. 60 (2021) 16085–16092, https://doi.org/10.1002/anie.202104001.

[35] X.-Z. Zhao, Y.-G. Xia, H.-P. Li, X. Wang, J. Wei, X.-L. Jiao, D.-R. Chen, Oxygen vacancy dependent photocatalytic CO$_2$ reduction activity in liquid-exfoliated atomically thin BiOCl nanosheets, Appl. Catal. B Environ. 297 (2021), 120426, https://doi.org/10.1016/j.apcatb.2021.120426.

[36] S. Das, J. Perez-Ranirez, J.-L. Gong, N. Dewangan, K. Hidajat, B.C. Gates, S. Kawi, Core–shell structured catalysts for thermocatalytic, photocatalytic, and electrocatalytic conversion of CO$_2$, Chem. Soc. Rev. 49 (2020) 2937–3004, https://doi.org/10.1039/c9cs00713j.

[37] X.-L. Yang, F.-F. Qian, G.-J. Zou, M.-L. Li, J.-R. Lu, Y.-M. Li, M.-T. Bao, Facile fabrication of acidified g-C$_3$N$_4$/g-C$_3$N$_4$ hybrids with enhanced photocatalysis performance under visible light irradiation, Appl. Catal. B Environ. 193 (2016) 22–35, https://doi.org/10.1016/j.apcatb.2016.03.060.

[38] B. Yang, X.-L. Li, Q. Zhang, X.-D. Yang, J.-G. Wan, G.-F. Liao, J.-J. Zhao, R.-J. Wang, J.-C. Liu, R.D. Rodriguez, X. Jia, Ultrathin porous carbon nitride nanosheets with well-tuned band structures via carbon vacancies and oxygen doping for significantly boosting H$_2$ production, Appl. Catal. B Environ. 314 (2022), 121521, https://doi.org/10.1016/j.apcatb.2022.121521.

[39] D.-D. Zhu, Q.-X. Zhou, Nitrogen doped g-C$_3$N$_4$ with the extremely narrow band gap for excellent photocatalytic activities under visible light, Appl. Catal. B Environ. 281 (2021) 119474, https://doi.org/10.1016/j.apcatb.2020.119474.

[40] M.K. Kumar, G. Naresh, V.V. Kumar, B.S. Vasista, B. Sasikumar, A. Venugopal, Improved H$_2$ yields over Cu-Ni-TiO$_2$ under solar light irradiation: behaviour of alloy nano particles on photocatalytic H$_2$O splitting, Appl. Catal. B Environ. 299 (2021), 120654, https://doi.org/10.1016/j.apcatb.2021.120654.

[41] S.-W. Cao, B.-J. Shen, T. Tong, J.-W. Fu, J.-G. Yu, 2D/2D heterojunction of ultrathin MXene/Bi$_2$WO$_6$ nanosheets for improved photocatalytic CO$_2$ reduction, Adv. Funct. Mater. 28 (2018) 1800136, https://doi.org/10.1002/adfm.201800136.

[42] J.-J. Wu, L.-J. Xiong, Y.-J. Hu, Y. Yang, X.-Y. Zhang, T.-Y. Wang, Z. Tang, A.-W. Sun, Y. Zhou, J.-Y. Shen, Z.-G. Zou, Organic half-metal derived erythroid-like BiVO$_4$/hm-C$_4$N$_3$ Z-Scheme photocatalyst: Reduction sites upgrading and rate-determining step modulation for overall CO$_2$ and H$_2$O conversion, Appl. Catal. B Environ. 295 (2021), 120277, https://doi.org/10.1016/j.apcatb.2021.120277.

[43] Y.-L. Wu, M.-Y. Qi, C.-L. Tan, Z.-R. Tang, Y.-J. Xu, Photocatalytic selective oxidation of aromatic alcohols coupled with hydrogen evolution over CdS/WO$_3$ composites, Chin. J. Catal. 43 (2022) 1851–1859, https://doi.org/10.1016/s1872-2067(21)63989-x.

[44] J. Xu, L.-W. Zhang, R. Shi, Y.-F. Zhu, Chemical exfoliation of graphitic carbon nitride for efficient heterogeneous photocatalysis, J. Mater. Chem. A 1 (2013), https://doi.org/10.1039/C3TA13188B, 14766-14722.

[45] B. Chai, J.-T. Yan, G.-Z. Fan, G.-S. Song, C.-L. Wang, In situ fabrication of CdMoO$_4$/g-C$_3$N$_4$ composites with improved charge separation and photocatalytic activity under visible light irradiation, Chin. J. Catal. 41 (2020) 170–179, https://doi.org/10.1016/s1872-2067(19)63383-8.

[46] L. Pan, S.-B. Wang, J.-W. Xie, L. Wang, X.-W. Zhang, J.-J. Zou, Constructing TiO$_2$ p-n homojunction for photoelectrochemical and photocatalytic hydrogen generation, Nano Energy 28 (2016) 296–303, https://doi.org/10.1016/j.nanoen.2016.08.054.

[47] S.-L. Wang, M. Xu, T.-Y. Peng, C.-X. Zhang, T. Li, I. Hussain, J.-Y. Wang, B.-E. Tan, Porous hypercrosslinked polymer-TiO$_2$-graphene composite photocatalysts for visible-light-driven CO$_2$ conversion, Nat. Commun. 10 (2019) 676, https://doi.org/10.1038/s41467-019-08651-x.

[48] Y. Wu, H. Wang, Y.-M. Sun, T. Xiao, W.-G. Tu, X.-Z. Yuan, G.-M. Zeng, S.-Z. Li, J. W. Chew, Photogenerated charge transfer via interfacial internal electric field for significantly improved photocatalysis in direct Z-scheme oxygen-doped carbon nitrogen/CoAl-layered double hydroxide heterojunction, Appl. Catal. B Environ. 227 (2018) 530–540, https://doi.org/10.1016/j.apcatb.2018.01.069.

[49] Z.-F. Wang, D.-Q. Chu, L.-M. Wang, L.-P. Wang, W.H. Hu, X.-Y. Chen, H.-F. Yang, J.-J. Sun, Facile synthesis of hierarchical double-shell WO3 microspheres with enhanced photocatalytic activity, Appl. Surf. Sci. 396 (2017) 492–496, https://doi.org/10.1016/j.apsusc.2016.10.181.

[50] X.-J. Luo, L. Qiao, S.-T. Zhang, Q.-J. Li, Y.-H. Liao, S.-C. Rao, H.-P. Liu, Y. Zhao, S-vacancy-assisted dual-sites on NiCo2S4 for photoconversion of CO$_2$ to olefiant gas, Appl. Surf. Sci. 601 (2022), 154184, https://doi.org/10.1016/j.apsusc.2022.154184.

[51] J.-X. Hao, D. Yang, J.-J. Wu, B.-X. Ni, L.-J. Wei, Q.-J. Xu, Y.-L. Min, H.-X. Li, Utilizing new metal phase nanocomposites deep photocatalytic conversion of CO$_2$ to C$_2$H$_4$, Chem. Eng. J. 423 (2021), 130190, https://doi.org/10.1016/j.cej.2021.130190.